Structural behaviour of unstabilized rammed earth constructions submitted to hygroscopic conditions

Bertrand François [*], Lucia Palazon, Pierre Gerard

Université libre de Bruxelles (ULB), BATir Department – Laboratory of GeoMechanics (LGM), Av. F Roosevelt 50 – CPI 194/02, 1050 Brussels, Belgium

HIGHLIGHTS

- We study the structural response of rammed earth construction (two-storey building).
- We perform a transient modelling of hygroscopic transfer through the wall.
- We consider the evolution of strength of the wall with hygroscopic conditions.
- We evaluate the effect of annual hygroscopic change on the structural behavior.
- We demonstrate the ability of rammed earth to support conventional loading.

ARTICLE INFO

ABSTRACT

Rammed earth constructions exhibit strength and deformation properties that evolve as a function of the relative humidity of the air in contact with the walls. This effect must be considered in the structural design of the construction. This work studies, through finite element simulation, the impact of the hygroscopic transfers through the wall on the structural response of a classical two-storey rammed earth building. The coupling between the mechanical and the hygroscopic behaviour is considered by the concept of effective stress for unsaturated soils, in order to reproduce the effect of suction on the strength, the stiffness and the volumetric variations of the rammed earth. The simulations show classical deformation of the structure due to distributed load on the floors while the hygroscopic changes in the rammed earth (essentially drying) induce additional displacements of the walls that remain in a very acceptable range. Finally, an extreme case is envisaged in which the loads on the floors are increased excessively in order to study the plastic response of the wall.

1. Introduction

Nowadays, earthen construction experiences an evident renascence thanks to numerous advantages of this material. Traditional construction techniques remain still relevant today but modern experimental methods and numerical modelling open large perspectives for the development of adequate standards for the design and the construction. Although this material demonstrates moderate mechanical performance, it remains largely sufficient for two-storey buildings. The local availability of the raw material, the low embodied energy and its potential for recycling [26,30] make this construction technique very attractive in the context of the development of circular economy. Hall & Allison [21] and Beckett & Cianco [4] demonstrated the efficiency of earthen materials to provide a natural hygrothermal regulation of the building.

Among different kinds of earthen constructions (see Houben & Guillaud [22] for an exhaustive review), rammed earth consists of compacting successive layers of soil inside a formwork to obtain a continuous and relatively homogeneous wall formed with compacted earth. "Unstabilized" rammed earth means that there are no additional binder elements (such as cement or lime). The use of natural soil without additive reduces the embodied energy and improves the recycling potential of the construction.

The strength of the construction is brought, for a part, by interlocking of soil particles induced by the compaction process that provides the required density [17]. Also, in addition, capillary cohesion, induced by the partial saturation of the earth, contributes, for a big part, to the resistance of the wall [16,25]. Consequently, the mechanical response of the unstabilized rammed earth, in terms of strength and deformability, is strongly affected by the

---

* Corresponding author.
 E-mail address: Bertrand.francois@ulb.ac.be (B. François).

hygroscopic conditions of the wall. All along the life of the building, the rammed earth wall will be submitted to evolving environmental conditions (the most important parameter being the air relative humidity) inducing transient hygroscopic transfers through the wall. The kinetics of water and vapor transfers through earthen walls was recently investigated numerically by Soudani et al. [34].

As a consequence of the continuous changes of water retention conditions, the stress-strain behaviour of the wall is permanently changing and their deformation and strength must be predicted as a function of the distribution of pore pressure conditions in the wall.

Since approximately one decade, the impact of the hygroscopic conditions on the mechanical behaviour of earthen construction is more and more investigated. Experimental studies show that the strength and the stiffness can be drastically increased when the earthen material is partially dried [7,8,24]. This effect of soil strengthening and stiffening is induced by internal suction that reinforces the contact between soil particles. Gerard et al. [18] deduced a unified failure criterion based on observed strength on unconfined compression and indirect tensile tests at different suction levels. The obtained failure criterion is based on the concept of effective stress for unsaturated soils that intrinsically includes the effect of suction and water retention properties inside the stress state [32].

The link between the mechanical behaviour of the rammed earth wall (in terms of strength and deformability) and the hygroscopic conditions should be considered in the design of such a structure through an approach that considers the hygromechanical coupling. Hygroscopic transfers through the wall control the suction distribution which, in turn, affects the mechanical response of the structure. Up to now, the design rules of rammed earth constructions are essentially based on empirical relations, physical properties of selected soil [13] or weak masonry guidelines that ignore those couplings. In most of the countries that established recommendations or standards, the only criterion related to rammed earth resistance consists in a characteristic value of unconfined compression strength under initial compacted conditions [29,33,35]. However, the evolution of this strength with the change of internal water content is never considered.

Very few attempts were initiated in the last years to quantify the structural behaviour of the wall taking hygroscopic conditions into account. Up to now, most of the approaches consider a constant and homogeneous water content profile in the whole structure [27,31]. In such a way, the mechanical properties of the wall are assumed homogeneous and the transient hygro-mechanical process is totally ignored. Furthermore, numerical modelling has also been used to quantify the structural behaviour of rammed earth wall submitted to seismic loading [6,27,28]. But still, the effect of hygroscopic conditions was not considered.

The present work proposes a hygro-mechanical finite element approach in order to reproduce those transient and highly nonlinear processes. The computations use a consistent hygro-mechanical framework for unsaturated soils in which the stiffness and the strength are controlled by suction. Transient behaviour is taken into account through the modelling of hygroscopic transfers through the wall. The strength and deformability of the soil is based on the experimental study performed by Gerard et al. [18] on a clayey silt relevant for unstabilized earth construction. The key parameters are the stiffness evolution as a function of the suction, the water retention curve that links the suction with the degree of saturation and the relative permeability that considers the change of water permeability as a function of the degree of saturation. The mechanical response of a typical two-storey building is considered along six years with representative atmospheric conditions in Belgium as boundary conditions at the wall faces.

2. Materials

In this study a clayey silt soil that has shown its relevance for earthen construction [18] is used. It comes from the region of Marches-Les-Dames (Belgium) and it consists of a clay of low plasticity (CL) according to the Unified Soil Classification System (USCS). Its index properties are: liquid limit (w_L = 32,5%; plasticity index (IP = 15%. The grain-size distribution curve is presented in Fig. 1. The clayey fraction represents 13%, the silty one about 61% and the sandy one about 26%. The grain size distribution of this clayey silt is very similar to the one suggested by Alley [3] to reach after compaction relevant soil dry density and strength for earthen constructions. Indeed the large spreading of the particle size distribution provides a good interlocking of the grains, and therefore good mechanical properties. A full mechanical characterization of this clayey silt can be found in Gerard et al. [18]. Here only the most relevant results are summarized and interpreted for the calibration of material parameters needed for the hygro-mechanical computations.

For sample preparation, the soil was dynamically compacted in three layers by sequentially ramming the soil in layers directly inside a mold of 36 mm in diameter and 72 mm in height. The compaction of each layer was achieved until the handle of the hammer "rings" when dropped onto the compacted soil, which is considered as the indication of full compaction having being attained [20,37]. In order to ensure repeatability of the sample preparation, we prepared a first sample with the criterion of the hammer that rings when dropped on the soil; we measured the density of the obtained sample; and then we repeated always the same density for all the samples (by controlling the mass of soil and volume of sample. The optimum water content at compaction was determined in order to obtain the highest unconfined compression strength. Those conditions were reached for a water content of 8% and a dry density of 2000 kg/m³. The suction of as-compacted samples, measured by the filter paper method [9], is equal to 2.4 MPa.

From those initial conditions, different suctions were applied to the samples through the control of relative humidity by different saline solutions [12]. Saturated saline solutions are installed at the bottom of a desiccator and adjust the water vapor concentration of the air (and so the relative humidity). Vapour exchange occurs between saline solution and soil samples placed in this desiccator (not in direct contact with the saline solution). The time necessary to reach equilibrium may be quite long. In our cases, it took from 5 to 25 days for the small samples and from 10 to 50 days for the biggest samples, depending on the imposed relative humidity.

The corresponding suction in the sample is obtained through the Kelvin's law:

$$s = -\frac{\rho_w RT}{M_w} \ln RH \tag{1}$$

where s is the suction, R is the constant of perfect gases (R = 8.3143 J/mol/K), T is the temperature in Kelvin (T = 293 K), M_w is the molar mass of water (M_w = 0.018 kg/mol), ρ_w is the bulk density of water (ρ_w = 1000 kg/m³), and RH is the relative humidity.

Table 1 reports the different applied suctions at a temperature of 20 °C. Note that the samples that reach the highest suction (125 MPa) have been dried under ambient conditions in a room where the temperature and humidity are constant.

Fig. 2a and b present the soil water retention curve expressed in terms of water content, w, and degree of saturation, S_r, respectively. Only water retention properties for suctions higher than initial suction were investigated because, as it will be demonstrated in the numerical modelling, during the life of the building, the
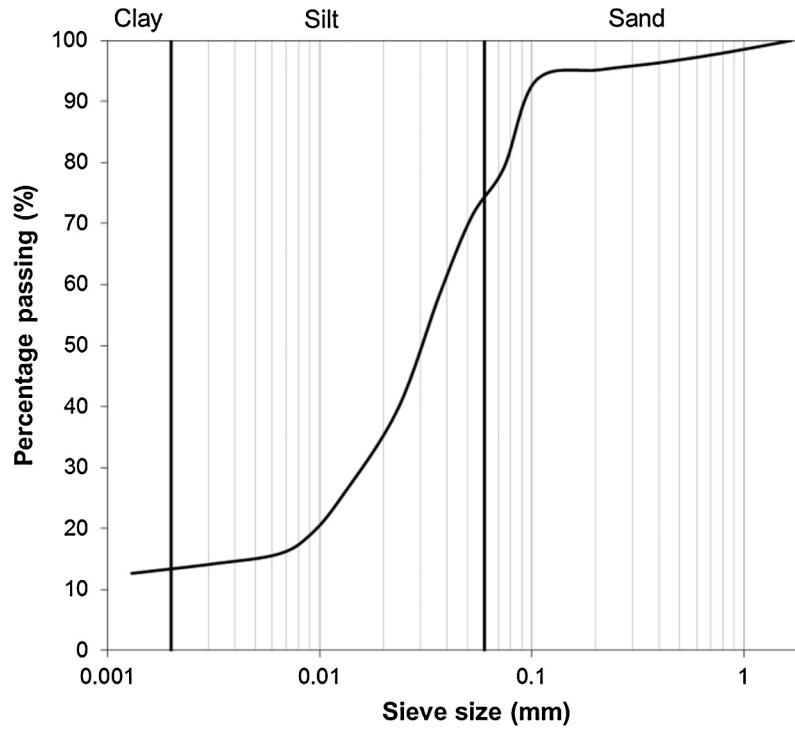
Fig. 1. Particle size distribution of the studied soil.

Table 1
Imposed suction for various saturated saline solutions at a temperature of 20 °C.
[1]Samples placed under ambient laboratory conditions.

Saturated saline solutions	Relative humidity RH (%)	Suction (MPa)
K_2SO_4	97	4.17
KNO_3	92	11.43
KCl	85	22.29
NaCl	75	39.46
(Ambient air)[1]	40	125

rammed earth is exclusively subject to suction higher than the initial suction of 2.4 MPa. It can be noted that the soil reaches very dry state (S_r = 12%) under ambient conditions. Water retention hysteresis upon wetting-drying was disregarded for the sake of

simplicity and also because the wetting and drying curves tend to coincide for low degree of saturation (close to the residual value).

At equilibrium with surrounding relative humidity, the height and 3 diameters (bottom, middle and top) were measured with a caliper for each sample. Fig. 3 presents the volumetric strain upon drying. Volumetric variations less than 1% are observed during a drastic drying at a relative humidity of 40%. This is not a huge deformation, but still it may have an impact on the global deformation of rammed earth structure upon drying. It is important to note that the addition of a small quantity of sand or gravel could have a positive impact on the reduction of shrinkage. But this has not been tested in the frame of this study.

Unconfined compression test are performed in order to determine the unconfined compressive strength (UCS) of soil samples
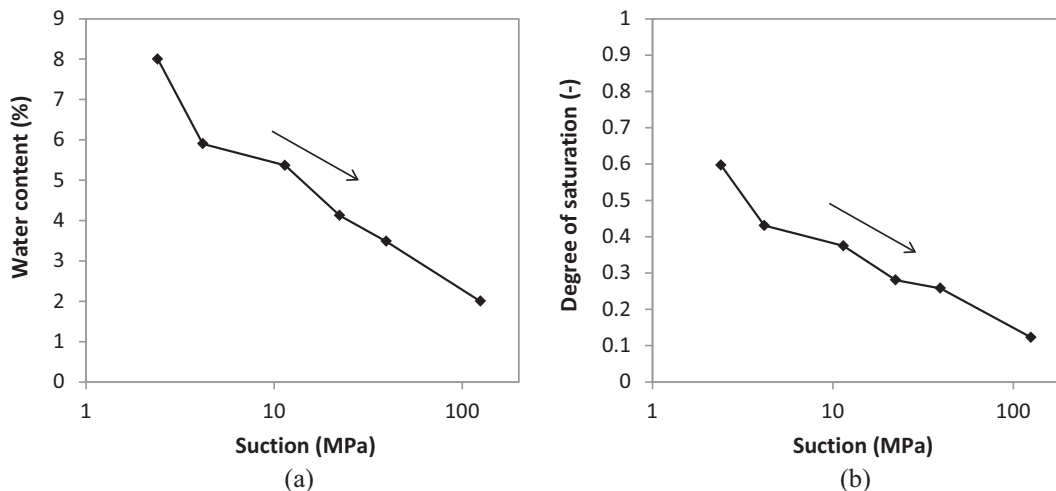

Fig. 2. Soil water retention curve (a) suction vs. water content and (b) suction vs. degree of saturation.
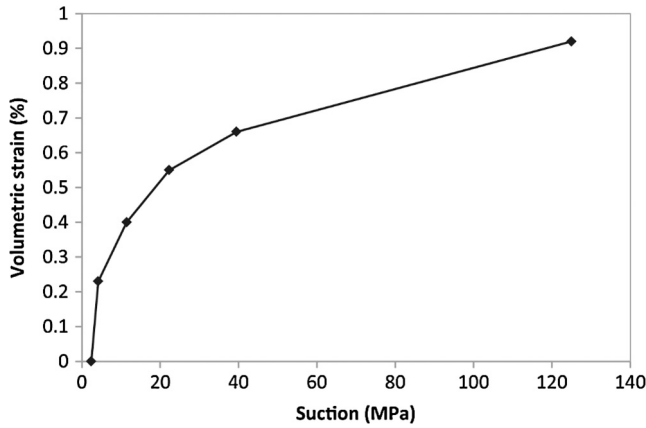
Fig. 3. Contractive volumetric strain upon drying from an initial suction of 2.4 MPa.

with unrestricted horizontal deformation. This is the most widely used measure of strength for rammed earth materials [37]. Tests were performed at the different suctions reported in Table 1. The stiffness modulus was obtained as the steepest slope of the axial stress – axial strain curve in a strain interval of 0.2% (i.e. the slope is obtained as a finite difference between +0.1% and −0.1% of strain around the considered point). The first part of the experimental curves shows a progressive mobilization of the stiffness before the maximum stiffness is observed. This is essentially an experimental artefact due to the progressive contact between the loading piston and the sample. This is not considered in the determination of the stiffness modulus. The Unconfined Compression Strength (UCS) is taken as the maximum axial stress reached. This method allows to deduce the two fundamental mechanical parameters used in the numerical modelling, with conventional soil mechanics tests.

UCS and stiffness modulus (E) are reported as a function of suction in Fig. 4a and b, respectively. For each suction, 2–4 unconfined compression tests were performed. The stiffness under saturated conditions has not been reported due to the plastic behaviour of the specimen. Except for the results at 4.17 MPa of suction, a logarithmic regression curve provides a good estimation of the obtained UCS and E. The low accuracy of the vapour transfer techniques at small suctions [12] can probably explain the out-of-trend strength and stiffness measured at a suction of 4.17 MPa.
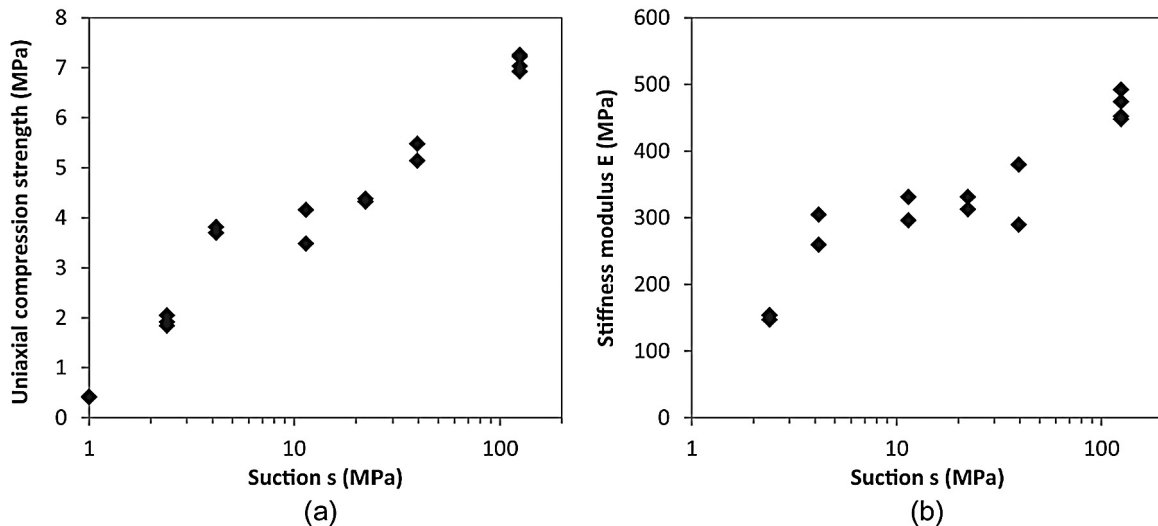
3. Hygro-mechanical laws

3.1. Balance equations

In this work, the hygro-mechanical behaviour of the rammed earth wall is addressed through finite element computations considering mechanical stress-strain behaviour and hygroscopic transfers. The LAGAMINE finite element code, including a thermo-hydro-mechanical finite element formulation [11,19], has been used.

The mechanical equilibrium is controlled by the momentum balance equation

$$\mathbf{div}(\boldsymbol{\sigma}) = 0 \tag{2}$$

where $\boldsymbol{\sigma}$ is the total stress tensor. In this work, the gravity is neglected and the total stresses are only induced by external loadings. This is justified by the moderate height of the building (6.4 m in total) that induces a self-weight of the wall much lower than the governing effective stress controlling the mechanical behavior of the wall (Eq. (3)).

At this stage, it is important to distinguish the total stress and the effective stress for unsaturated soils. The total stress distribution fulfills the global equilibrium of the structure while the effective stress $\{\boldsymbol{\sigma}'\}$ is a combination of the total stress and the internal pore pressure [5,32]:

$$\boldsymbol{\sigma}' = \boldsymbol{\sigma} + \chi s\mathbf{I} = \boldsymbol{\sigma} + (S_r)^\alpha s\mathbf{I} \tag{3}$$

where $\mathbf{I}$ is the identity matrix and s the suction that is the difference between air and water pressure ($s = p_a - p_w$). In this expression, it has been decided to use an hyperbolic function of the degree of saturation S_r for the expression of the effective stress parameter χ, as suggested by Alonso et al. [2]. α is a material parameter.

The equilibrium and balance equations, as well as the water flow, are expressed in the moving current configuration through a Lagrangian actualized formulation [10] with the consequence that there is no evolution of solid skeleton mass and the mass is conserved in any given reference volume:

$$\frac{\partial}{\partial t}(\rho_s(1-n)) = 0 \tag{4}$$

where ρ_s is the bulk density of solid grains, n the soil porosity and t the time.

Fig. 4. (a) Unconfined compression strength and (b) stiffness modulus of the tested soils as a function of suction.
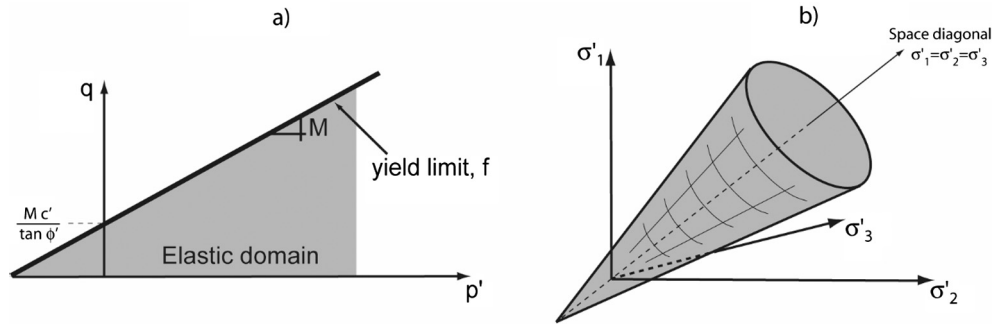
Fig. 5. Yield limit of the Drucker-Prager model: (a) View in the (p'–q) plane and (b) in the principal stress space.
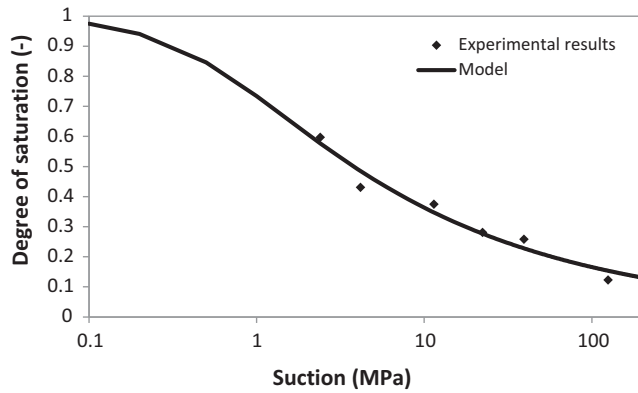

Fig. 6. Water retention curve. Best fitting between Van Genuchten's equation and experimental results.
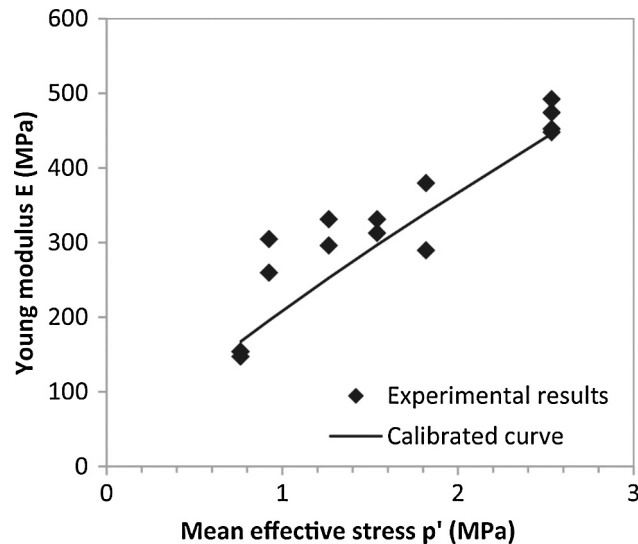

Fig. 7. Calibration of non-linear elasticity based on elastic stiffness measured on unconfined compression test. The Young modulus is a function of the mean effective stress (Eq. (7)), affected by the suction level.

The water mass balance equation translates the equilibrium between water (liquid water and water vapour) in- and out-flow and the storage coefficient that may come from a variation of the degree of saturation, a variation of porosity or a change of bulk density of liquid water ρ_w or water vapour ρ_v.

$$\frac{\partial}{\partial t}(\rho_w n S_r + \rho_v n(1 - S_r)) + div(\mathbf{f_w}) - Q_w = 0 \qquad (5)$$

Table 2
reports the calibrated materials parameters.

Parameters	Symbols	Units	Values
Young modulus at reference mean effective stress p'_{ref} = 1 MPa	E_{ref}	MPa	208
Non-linear elasticity exponent	n^e	–	0.81
Poisson coefficient	v	–	0.25 (*)
Friction angle	ϕ'	°	36.5
Cohesion	c'	kPa	6.2
Dilatancy angle	ψ	°	0 (*)
Exponent of effective stress parameter	α	–	2.08
Coefficient of the Van Genuchten water retention curve	n_w	–	1.325
Coefficient of the Van Genuchten water retention curve	α_w	MPa	0.528
Coefficient of the Van Genuchten water retention curve	$S_{r,res}$	–	0
Coefficient of permeability	k_w^{sat}	m²	5.54 10^{-16}
Porosity	N	–	0.26
Tortuosity	τ	–	0.50

$\mathbf{f_w}$ is the mass flow. Q_w is a volume source of water. Isothermal conditions are assumed so that the thermal transfer through the wall is ignored.

3.2. Constitutive equations

To relate the unknowns included in the balance equations with the primary unknowns of the finite element problem (i.e. the x and y displacements and the pore water pressure p_w), a series of constitutive equations are required.

First, the strains are linked to the variation of effective stress through a Drucker-Prager elasto-plastic constitutive model. The strain rate is decomposed into elastic $\mathbf{d}\varepsilon^e$ and plastic $\mathbf{d}\varepsilon^p$ strain rate:

$$\mathbf{d}\varepsilon = \mathbf{d}\varepsilon^e + \mathbf{d}\varepsilon^p \qquad (6)$$

The elastic component of the strain is governed through a non-linear hypoelastic law where the Young modulus E is a function of the mean effective stress through a hyperbolic function as used by François & Laloui [15] see also Hujeux [23]:

$$E = E_{ref}\left(\frac{p'}{p'_{ref}}\right)^{n^e} \qquad (7)$$

where p' is the mean effective stress. E_{ref} is the reference Young modulus at the reference mean effective stress, p'_{ref} (= 1 MPa in our case). n^e is a material parameter.

The mechanical behaviour is assumed elastic-perfectly plastic: the material response is fully elastic up to the yield limit that cor-
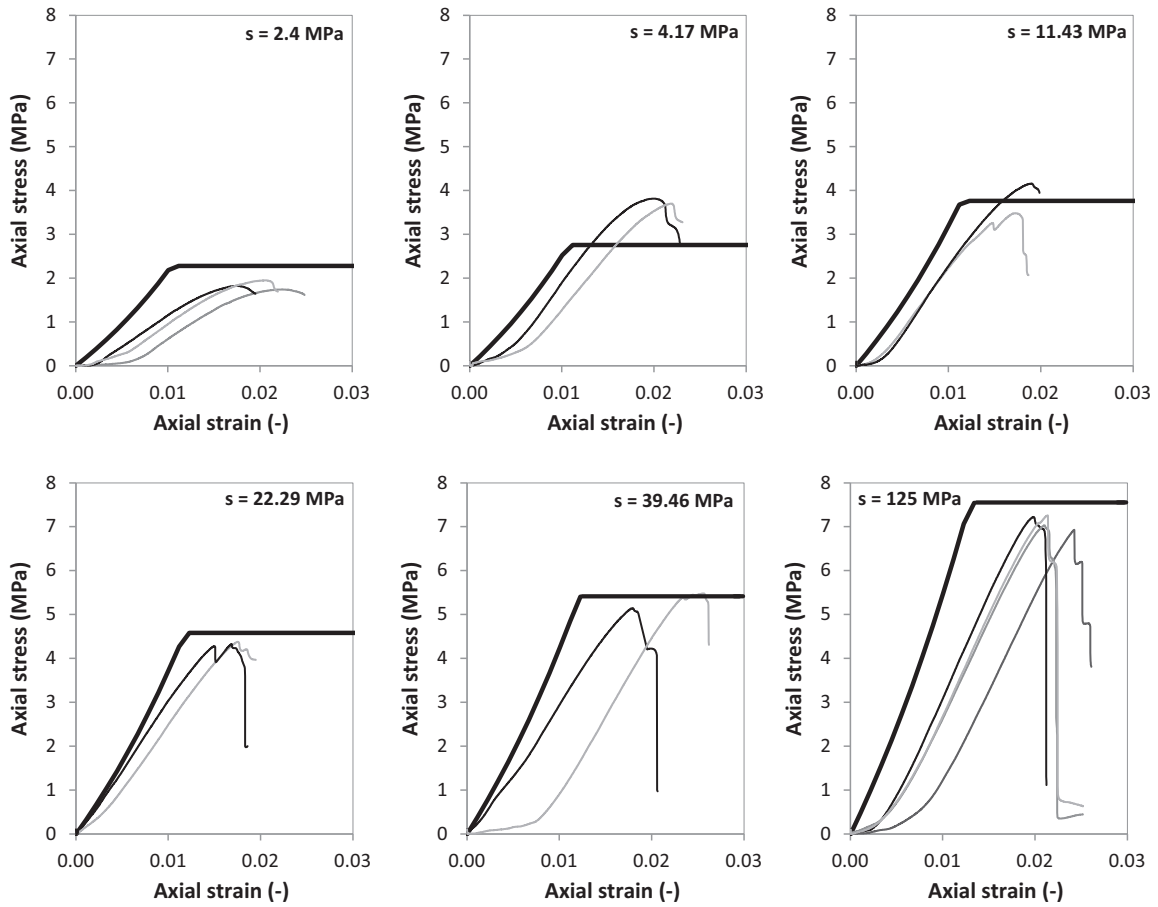
Fig. 8. Unconfined compression tests at different suctions. The non-linear elastic perfectly plastic model is able to reproduce the effect of suction on stiffness and ultimate strength. Thick curves: Model prediction; Thin curves: Experimental results.
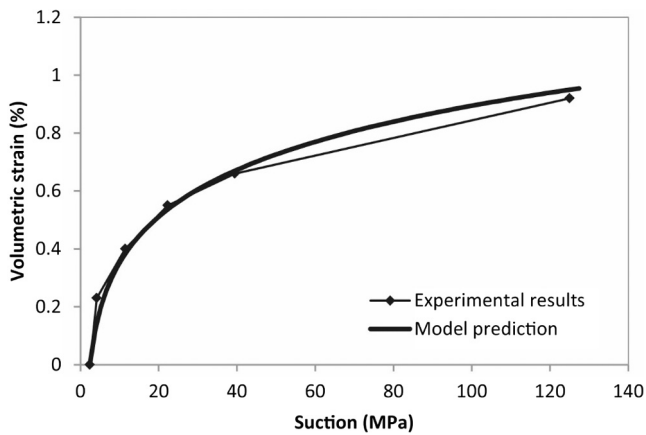

Fig. 9. Volumetric strain upon drying: Comparison between experimental results and model prediction. It is to note that the model prediction would be fully reversible upon re-wetting.

responds to the failure limit. A Drucker–Prager failure surface is adopted [14] (Fig. 5):

$$f \equiv q - M\left(p' + \frac{c'}{\tan \phi'}\right) = 0 \tag{8}$$

with

$$M = \frac{6 \sin \phi'}{3 - \sin \phi'} \tag{9}$$

p' and q are the mean effective stress and the deviatoric stress and c' and ϕ' are the cohesion and the friction angle, respectively.

Once the failure criterion is reached, the plastic strains are determined through the plastic multiplier $d\lambda$ and the derivative of the plastic potential g:

$$\mathbf{d}\varepsilon^{\mathbf{p}} = d\lambda \frac{\partial g}{\partial \boldsymbol{\sigma}} \tag{10}$$

with the plastic potential g:

$$g \equiv q - M'p' = 0 \tag{11}$$

with

$$M' = \frac{6 \sin \psi}{3 - \sin \psi} \tag{12}$$

where ψ is the dilatancy angle.

The mass flow $\mathbf{f_w}$ is defined as the sum of the advection of the liquid water (generalized Darcy's law for unsaturated conditions) and the diffusion of water vapour (Fick's diffusion law):

$$\mathbf{f}_w = -\rho_w \frac{k_w^{sat} k_{w,r}}{\mu_w}(\mathbf{grad}(p_w)) - D\tau n(1 - S_r)(\mathbf{grad}(\rho_v)) \tag{13}$$

where k_w^{sat} is the intrinsic permeability under saturated conditions, $k_{w,r}$ is the relative permeability (see Eq. (15)), μ_w the dynamic viscosity of water ($\mu_w = 0.001$ Pa·s), D is the molecular diffusion of the mixture water vapour – air ($D = 2.78\ 10^{-5}$ m^2/s), τ is the tortuosity.

Classically under partially saturated conditions, a water retention curve and a water permeability curve are defined to relate the degree of saturation with suction (i.e. negative pore water pressure) and the water permeability with the degree of saturation, respectively. These relationships are based on the van Genuchten's equation [36]:

$$S_r = \left(1 + \left(\frac{(s)}{\alpha_w}\right)^{n_w}\right)^{\frac{n_w}{n_w-1}} \tag{14}$$

$$k_{w,r} = \sqrt{S_r}\left(1 - \left(1 - (S_r)^{\frac{1}{1-n_w}}\right)^{\frac{n_w-1}{n_w}}\right)^2 \tag{15}$$

where n_w and α_w are material parameters.

4. Material parameters

The coupled hygro-mechanical model is able to reproduce a series of coupling processes between the hydraulic behaviour (i.e. water migration through the wall) and the mechanical behaviour (stiffness and strength). Parameters are calibrated based on laboratory tests as follows.

Fig. 6 reproduces the best fitted Van Genuchten's water retention curve in comparison with the experimental curve, in the least square sense. Then, following the work of Gerard et al. [18], the effective stress parameter is a hyperbolic function of the degree of saturation (Eq. (3)) in order to obtain a unified failure criterion at different suction levels. According to this work performed on the same material, at the same density, the unified failure criterion is obtained for an exponent $\alpha = 2.08$. Also, according to non-linear elasticity (Eq. (7)), the evolution of effective stress with suction also reproduces the stiffening of the materials when suction increases (dry material is usually stiffer than wet material). The Young modulus is a function of the mean effective stress which is affected by the suction level, while the Poisson ratio is assumed constant. The two parameters of Eq. (7) are calibrated based on the elastic stiffness observed along unconfined compression tests (Fig. 4b). The water retention curve and the expression of effective stress being known, it is possible to relate the suction level to the mean effective stress. Fig. 7 reports the measured Young modulus as a function of the mean effective stress, as well as the calibrated evolution of this Young modulus using Eq. (7). The best fit in the least square sense is obtained for $n^e = 0.81$ and $E_0 = 208$ MPa.

The intrinsic permeability in saturated conditions has been evaluated experimentally to 5.54×10^{-16} m² with a falling head permeameter. According to Van Genuchten [36], it is assumed that the relative permeability coefficient that controls the evolution of the permeability with the degree of saturation can be directly obtained from the retention curve parameters. So, the coefficient n_w of Eq. (15) (relative permeability equation) is deduced from the calibration of Eq. (14) (water retention curve equation).

Table 2 Materials parameters. (∗) Without accurate data about Poisson coefficient and dilatancy angle, usual values have been chosen, by default.

Fig. 8 shows the ability of the model to predict the stress-strain response of the material upon unconfined compression tests at different suctions. In particular, the increase of stiffness and strength when suction increases is well reproduced thanks to the combination of non-linear elasticity and generalized effective stress. When suction is modified, the effective stress changes (Eq. (3)) which has an impact on the failure criterion (Eq. (8)) and the elastic stiffness (Eq. (7)). The experimental artefact at the start of the curves linked to the progressive mobilization of the contact between the loading piston and the sample, not linked to the intrinsic response of the material, is not considered by the model. As a consequence of the elastic, perfectly-plastic model, the post-peak response is modelled

as a constant deviatoric stress while the experimental response shows a brittle failure (not considered by the model). Actually, brittle post-peak response is very delicate to tackle by numerical model because of bifurcation process and non-unicity of the solution. The main objective of the present work being to study the
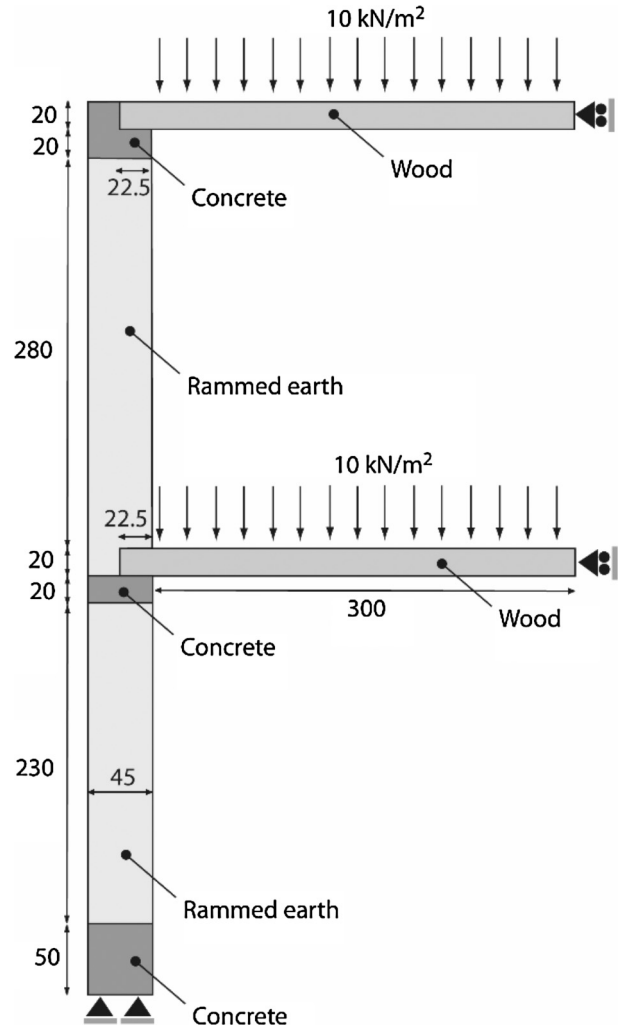

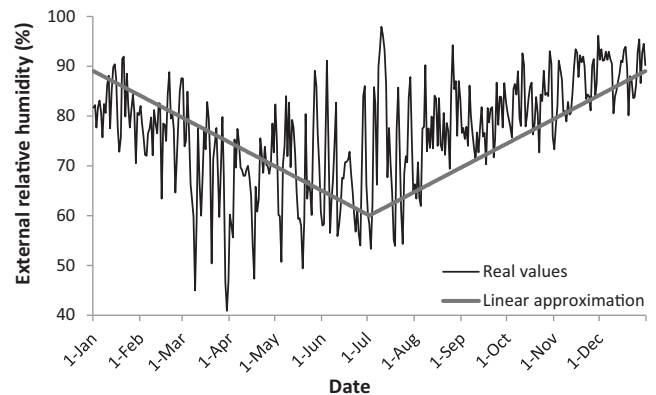**Fig. 10.** Considered geometry of the case study. Dimensions are in cm.

Fig. 11. Daily evolution of the external air relative humidity as observed in Uccle Observatory (Belgium) during the year 2014. This condition is applied according to the bi-linear fitting as the boundary condition on the external wall face. The same evolution is repeated during 6 years.
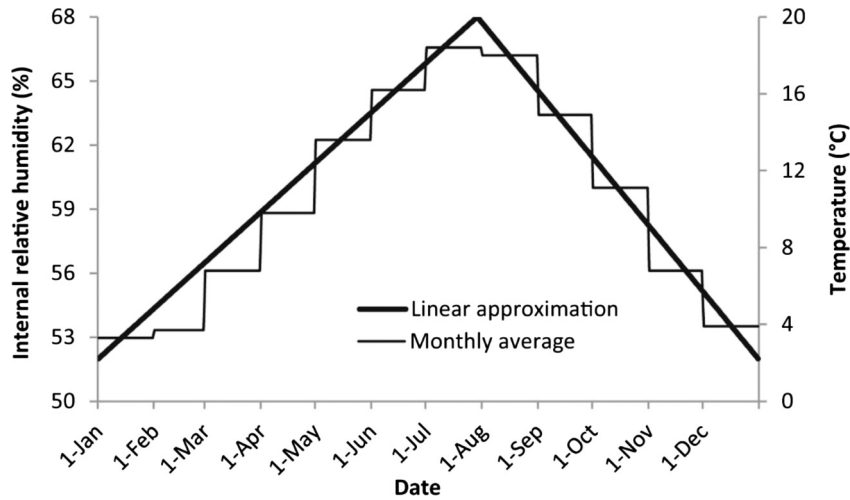
Fig. 12. Linear approximation of the monthly average external temperature, as recorded at the meteorological observatory of Uccle (Belgium). The internal relative humidity is linked to external temperature through a linear one-to-one relationship (Eq. (16), when T = 0 °C, RH = 50% and when T = 20 °C, RH = 68%).
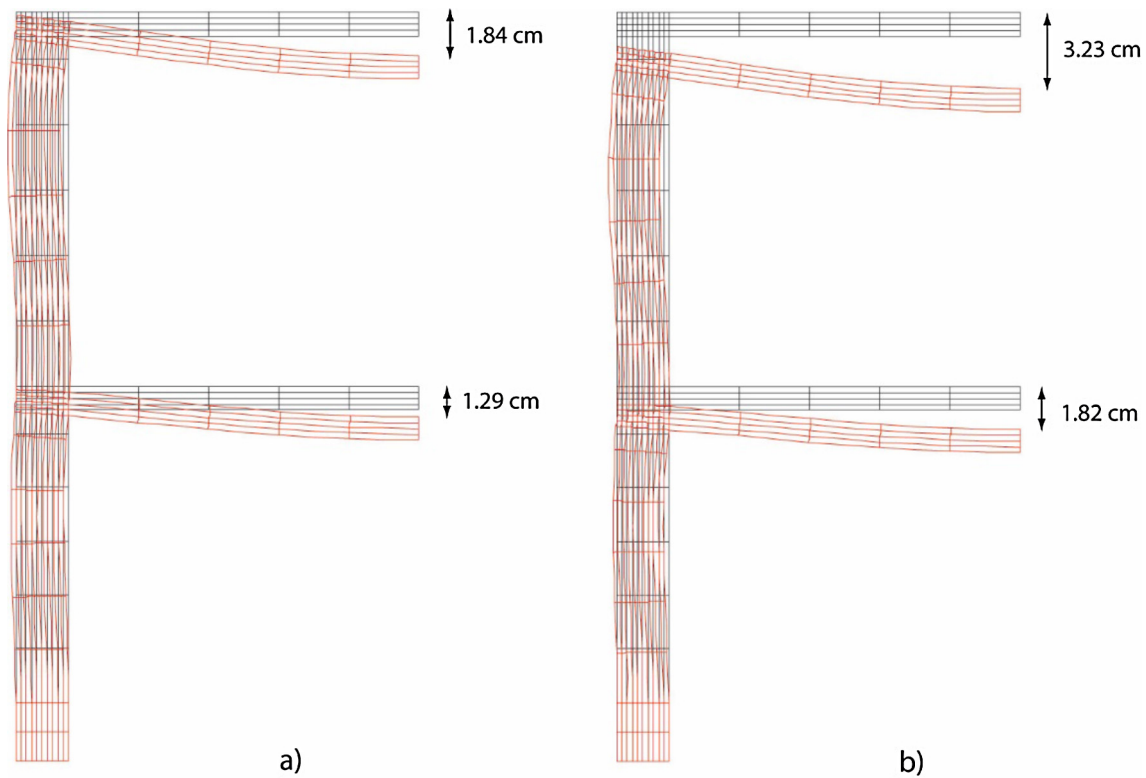

Fig. 13. Deformed structure (a) after the application of the pressure on floors at time t = 0 and (b) at the end of the 6th year of simulation. Amplification of the displacement: 20.

behaviour of the structure upon serviceability loading, the aspect related to failure processes are out of the scope of this paper and the failure limit is used as a criterion to evaluate how far we are from the critical situation.

In parallel, this non-linear elasticity coupled with the effective stress is also able to tackle the volumetric change upon drying, as demonstrated in Fig. 9. The matching between experimental results and model prediction is particularly noticeable because the model results consist exclusively in blind prediction. The parameters were calibrated on the water retention curve (for the hygroscopic behaviour) and the unconfined compression tests (for the mechanical behaviour) and the response upon drying is a consequence of the coupling between the mechanical and hygro-

scopic behaviours. Upon low suctions, the stiffness is relatively limited which generates significant volumetric strain upon drying at low suctions. Then, when suction increases, the material becomes stiffer and the slope of the volumetric strain vs suction curve is progressively reduced.

5. Case study

We consider a classical two-storey building (a ground floor plus a first floor) supported by 45 cm thick rammed earth external walls with two 6 m span floors made of wood. At the connection between slabs and walls, a piece of concrete is placed to avoid

stress concentration at the contact between wood and rammed earth. Also, the base course of the wall is made of concrete on a height of 50 cm. Those construction techniques are conventional for rammed earth building [22]. The problem is studied in two dimensions and only half of the structure is considered for symmetry reason. Fig. 10 shows the considered geometry.

The rammed earth properties are taken from the experimental studies above (see Table 2) while the properties of concrete and wood are conventional. We neglect the hygroscopic transfers in those two materials (i.e. the governing stress is the total stress) and the mechanical response of those two materials is assumed linear elastic ($E_{concrete}$ = 20 GPa; $\nu_{concrete}$ = 0.15; E_{wood} = 11 GPa; ν_{wood} = 0.25).

5.1. Boundary conditions

Hydraulic conditions are applied as an imposed water pressure at the wall faces. For the external conditions, the evolution of air relative humidity during the year 2014 collected in the observatory of Uccle (Belgium) is considered. To evaluate the behaviour of the structure during several years, the same annual conditions are repeated during 6 years. The simulation starts in January. The daily values evolving along the year are fitted by a bi-linear curve, as indicated in Fig. 11. The internal relative humidity in the building is deduced from the external temperature, recorded in the meteorological observatory of Uccle (Belgium), according to the relation proposed by AASHRAE Tenworld [1]:

$$RH_{int} = 50 + \frac{18}{20} T_{ext} \qquad (16)$$

where RH_{int} is the internal relative humidity expressed in percent and T_{ext} is the external temperature, expressed in °C. According to AASHRAE Tenworld (2008), this relation is valid from −10 °C to 20 °C. Fig. 12 plots the obtained internal relative humidity.

Once the relative humidities are known on both faces of the wall, the corresponding negative water pressures can be deduced from the Kelvin's law (Eq. (1)).

The mechanical boundary conditions reproduce the fixed displacement in the horizontal and vertical directions at the level of the foundation, the fixed horizontal displacement at the symmetry axis and the uniformly distributed pressures on the floors (vertical pressure of 10 kN/m² corresponding to permanent and temporary loads).

The mechanical load is immediately applied at the beginning of the simulation and is maintained all along the process. So, at time t_0 the displacement in the structure are only due to the mechanical loading (10 kN/m² on each floor) and then the displacements evolve due to the evolution of the hydraulic conditions in the structure induced by climatic changes on both faces of the wall. This immediate application of the load is the most severe case because the load is applied on the wall at its wetter and softer state. So, as an alternative, we have also considered another case where the load is applied after 6 month of drying (the end of construction is in January while the loading is applied in July).

5.2. Results on conventional loading

Initially, the uniformly distributed pressure on the floors produces a deflection of the structure induced by the bending of the slabs and the wall (Fig. 13a). The maximum vertical displacement at mid-span is 1.84 cm for the top floor and 1.29 cm for the bottom floor. The connections between slab and wall slightly rotate due to the flexibility of the wall.

In summer, the external environment is dry (s = 69 MPa; RH = 60%) while the internal condition is wetter (s = 52 MPa; RH = 68%). In winter, the conditions are reversed: s = 16 MPa

(RH = 89%) and s = 88 MPa (RH = 52%) for external and internal conditions, respectively. Consequently, the wall is continuously submitted to hygroscopic changes. Fig. 14 shows the profile of the suction through the wall at a height of 5 m in January and July during the 6 years of simulation. During the first years of simulation, the suction in the core of the wall increases significantly because the environmental conditions are much dryer than the initial conditions of the rammed earth after compaction. Then, after a few years, the core of the wall is still drying but more gently while
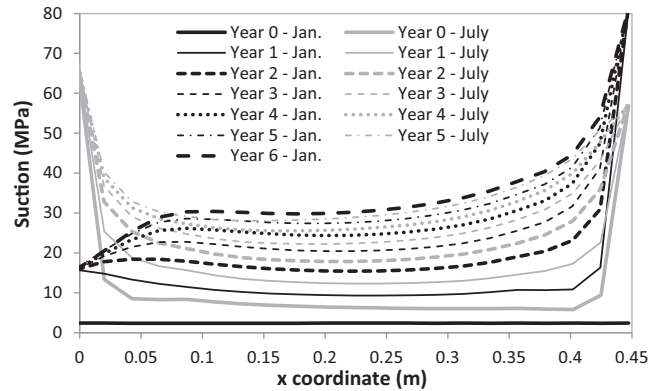

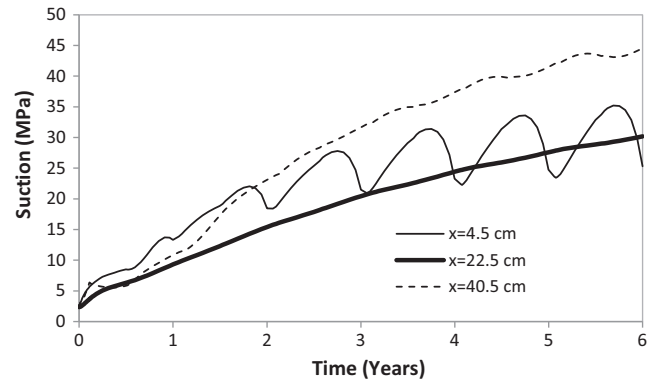**Fig. 14.** Profile of suction through the wall at a height of 5 m in January and June during 6 years.

Fig. 15. Evolution of suction in the middle of the wall (x = 22.5 cm) and close to both faces (x = 4.5 cm: at 4.5 cm from the external wall and x = 40.5 cm at 4.5 cm from the internal wall) at a height of 5 m during the 6 years of simulation.
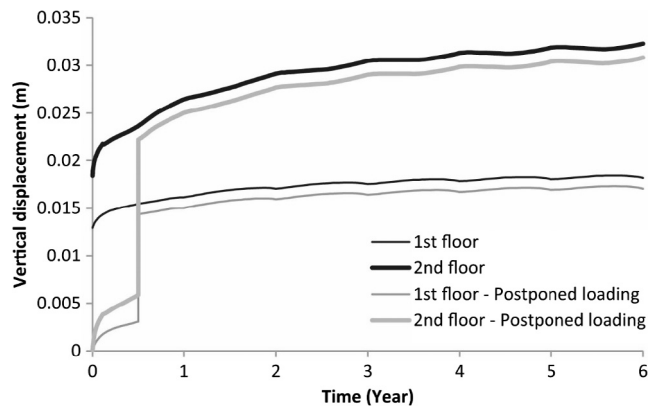

Fig. 16. Evolution of the vertical displacements at the mid-span of the two floors for the basic case (application of the load at time t = 0) and for the case with postponed loading (loading after 6 months of construction).
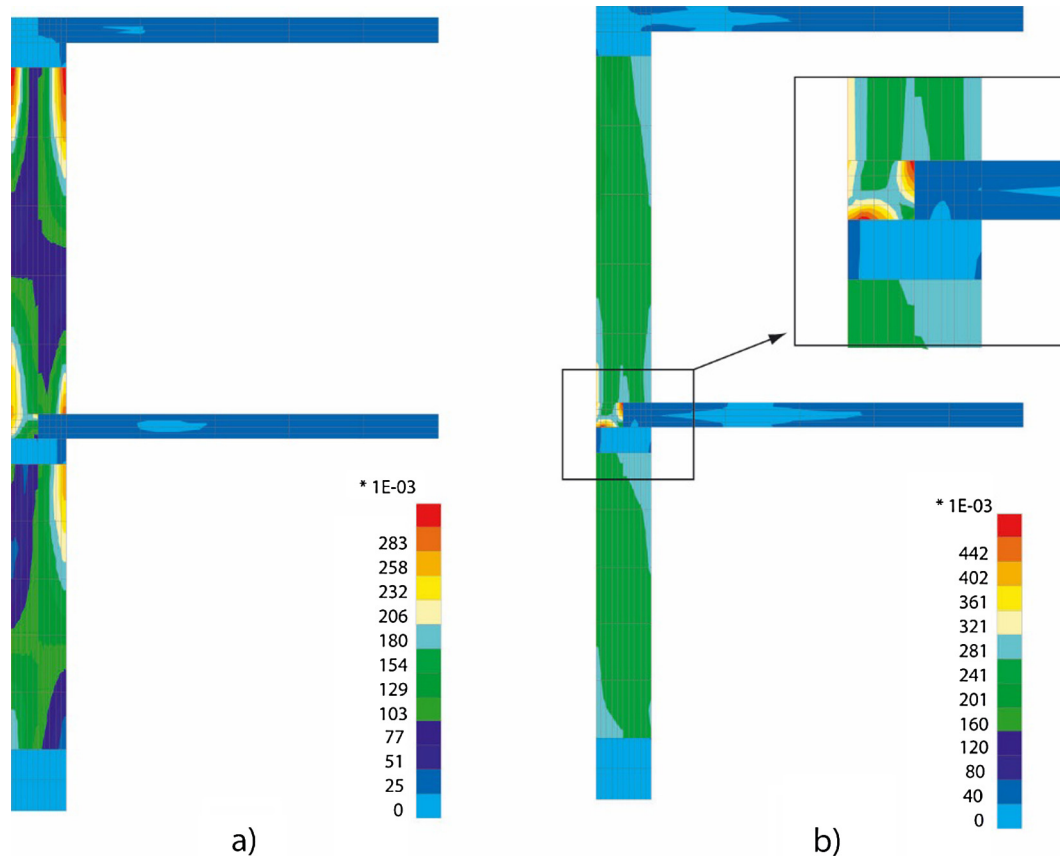
Fig. 17. Map of plastic indicator in the structure (a) after the application of the pressure on floors and (b) at the end of the 6th year of simulation for the standard loading (10 kN/m^2 on the floors).

the suction change are still noticeable near the external face, on a skin of around 5 cm thickness. This is confirmed by Fig. 15 that shows the evolution of suction at the same height in the middle and close to both faces of the wall during the 6 years of simulation. It is observed that the middle of the wall is still continuously drying and 6 years are not enough to reach a kind of steady state. Time required to reach a constant hygroscopic condition in the middle of the wall depends on the permeability of the soil, the thickness of the wall and the climatic conditions.

In terms of displacements, the global drying of the rammed earth produces a shrinkage of the materials that generates a vertical displacement of the structure increasing from the bottom to the top. Consequently, the 1.84 cm of displacement induced by the distributed pressure on the floors at time t = 0 increases up to 3.23 cm after 6 years due to rammed earth shrinkage (Fig. 12b). The shape of the deformed configuration does not change significantly. Only the wall is shortened of approximately 1.4 cm. Fig. 16 shows the evolution of the vertical displacement at the mid-span of the two floors during the 6 years of simulation. After the initial deflection due to the immediate mechanical loading, the displacement still increases due to shrinkage of the wall. However, this process tends progressively to stabilize because the suction change in the core of the wall is slower with time. Small oscillations are observed due to the annual cycles of the environmental conditions.

As an alternative, we have also considered the loading of the floors 6 months after the construction. In this case, the wall had already time for partial drying. Consequently the wall is stiffer and the induced displacement is slightly reduced. The vertical displacement of the top floor at the end of the process is now reduced to 3.08 cm (instead of 3.23 cm when the load is applied immediately).

All along the process, the structure is really far from failure. Fig. 17 shows the plastic indicator *PI* that is the ratio between the current deviatoric stress and the deviatoric stress corresponding to failure for the same mean effective stress:

$$PI = \frac{q}{q_{failure}} \tag{17}$$

This parameter is a local indicator of how far the considered point is from failure. When *PI = 1*, the stress state is upon the failure criterion. As demonstrated in Fig. 17, the plastic indicator remains lower than 0.5 all along the process. After the loading of the floors (Fig. 17a), the maximum *PI* are located at the top of the wall close to both faces. This is due to the bending of the wall that generates uniaxial tension and compression on the sides of the wall. Then, in the bulk of the wall the plastic indicator is increased between time t = 0 (IP = 0.08) and after 6 years of simulation (IP = 0.2). This is due to the gradient of suction in the wall that produces a gradient of effective stress which in turn induces deviatoric stress. Also, at the connection between the wall and the first floor (Fig. 17b) the IP values are slightly increased because the differential shrinkage between rammed earth and wood produces some shear stresses. However, the IP values remains in very acceptable limits everywhere.

5.3. Results up to plastic state

Let's now imagine an extreme situation where the pressure on the floors would induce a state very close to failure. When a pressure of 80 kN/m^2 (eight times the recommended maximum pressure in usual standards) is applied on the floors, plastic hinges are generated at the top and the bottom of the first floor wall
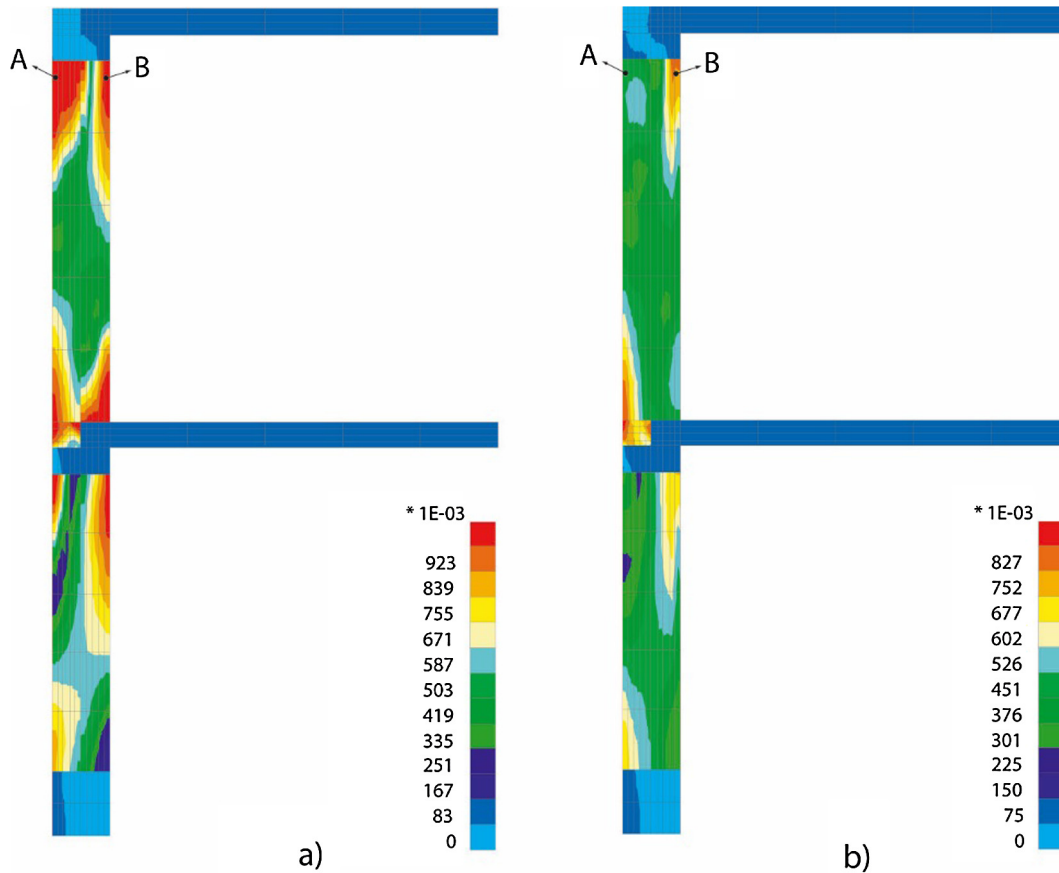
Fig. 18. Map of plastic indicator in the structure (a) after the application of the pressure on slabs and (b) at the end of the 6th year of simulation for an extreme loading (80 kN/m^2 on the slabs). Points A and B are the locations where the stress path is followed in Fig. 19.
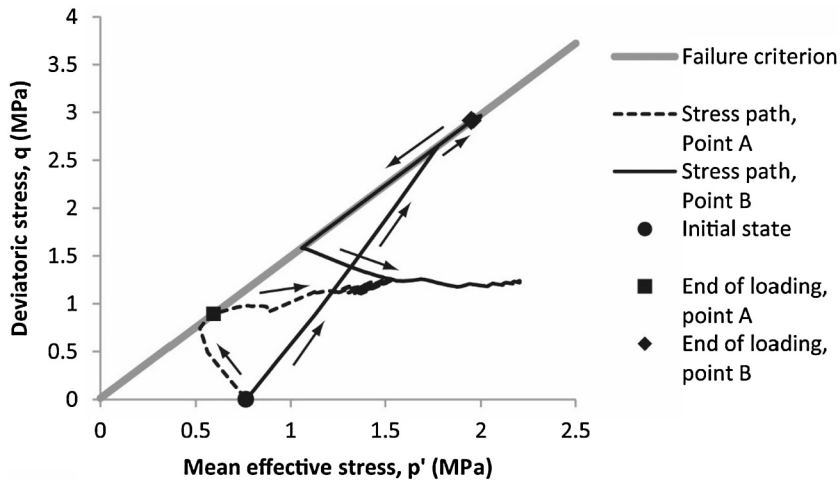

Fig. 19. Stress paths followed in the p'-q plane by points A and B (their locations are reported in Fig. 18) during the extreme loading on the floors and the 6 years of simulation.

(Fig. 18a). The plastic indicator is equal to one almost everywhere in those two zones that is characteristic of a situation close to failure. However, along the drying process of the wall (during the 6 years of simulation), the evolution of the plastic indicator is favorable for the stability of the structure. It decreases everywhere and comes back to value significantly smaller than one that indicates an elastic response without any failure zone in the structure (Fig. 18b). This is due to the drying process that strengthens the rammed earth. This process is demonstrated in Fig. 19 where the

stress path of two points located in the more sensitive zone (in the initial plastic hinges) is drawn in the (p'-q) plane together with the failure criterion. The locations of the two points (A and B) are reported in Fig. 18. One point is located in the side of the wall in tension (close to the external face, point A) while the other point is in the compressed side of the wall (close to the internal face, point B). During the loading on the floors, point A is essentially submitted to a triaxial extension loading path (the vertical stress is reduced while the horizontal stress remains constant) while

point B is submitted to triaxial compression loading path (the vertical stress increases while the horizontal stress remains constant). Both points reach the failure criterion rapidly before the end of the loading phase. However, during the drying process, the increase of mean effective stress (induced by the increase of suction (see Eq. (3))) produces a displacement of the stress point toward the elastic domain (far away from the failure criterion).

6. Conclusions

Rammed earth is a material which may be strongly affected by the hygroscopic conditions. The material strength and stiffness are constantly evolving due to the change of hygroscopic environmental conditions. To obtain good compaction, the rammed earth is relatively wet at the moment of construction and tends to dry with time. The drying is faster on the sides of the wall in direct contact with the environmental conditions while the core remains wetter. Several annual cycles are needed to dry the material in the middle of the wall. The speed of those hygroscopic transfers is controlled by the permeability of the material.

It is essential to characterize this hygroscopic behaviour because it has a strong influence on the structural response of the rammed earth wall, in terms of deformation and failure. Dryer is the material and higher are the stiffness and strength.

This coupled hygro-mechanical behaviour in a rammed earth wall has been addressed through finite element computations. Hygroscopic transfers follow the Darcy's law extended to unsaturated soils in which the water permeability is a function of the degree of saturation. The mechanical behaviour is directly coupled to the hygroscopic conditions through the effective stress for unsaturated soil. Non-linear elasticity takes into account the stiffening of the material when it is dried.

The hygro-mechanical model has been calibrated based on relatively conventional soil mechanics laboratory tests. Unconfined compression tests at different controlled suctions (imposed by relative humidity techniques) and shrinkage measurements upon drying are enough to obtain the relevant parameters of the model. This straightforward experimental procedure can be carried out in any conventional laboratory of soil mechanics.

A typical two-storey rammed earth building has been considered as a case study. The problem has been addressed in two dimensions. A uniform load of 10 kN/m^2 applied on the floors produces classical bending and contraction of the walls without local failure. Additionally, the hygroscopic changes in the wall produce further settlements induced by the material drying. It is observed that the structure is continuously evolving because of the endless change of the hygroscopic environmental conditions but the global trend is essentially drying during the 6 first years, in a Belgian climate.

In order to evaluate the ultimate bearing capacity of the rammed earth structure, an extreme case with a load of 80 kN/m^2 on the floors has been simulated. The results show that plastic hinges are created in the wall but those plastic zones disappear and the behaviour comes back into the elastic regime when the wall dries. From a practical point of view, it indicates that time plays a positive role for the stability of the earthen structure due to material drying. Consequently, the walls may resist to important load (much higher than the recommended maximum loading in usual standards) several years after the construction.

References

[1] AASHRAE TenWolde, Standard 160P: criteria for moisture control design analysis in buildings, ASHRAE Trans. 114 (1) (2008) 167–169.
[2] E.E. Alonso, J.M. Pereira, J. Vaunat, S. Olivella, A microstructurally based effective stress for unsaturated soils, Géotechnique 60 (12) (2010) 913–925.
[3] P.J. Alley, Rammed earth construction, N. Z. Eng. 3 (6) (1948) 582.
[4] C. Beckett, D. Ciancio, A review of the contribution of thermal mass to thermal comfort in rammed earth structures, in: 2nd International Conference on Sustainable Built Environment, Sri Lanka, 2012.
[5] A.W. Bishop, The principle of effective stress, Tecnisk Ukeblad 39 (1959) 859–863.
[6] T.T. Bui, Q.B. Bui, A. Limam, J.C. Morel, Modeling rammed earth wall using discrete element method, Continuum Mech. Thermodyn. 28 (1–2) (2016) 523–538.
[7] Q.B. Bui, J.C. Morel, S. Hans, P. Walker, Effect of moisture content on the mechanical characteristics of rammed earth, Constr. Build. Mater. 54 (2014) 163–169.
[8] F. Champiré, A. Fabbri, J.C. Morel, H. Wong, F. McGregor, Impact of relative humidity on the mechanical behavior of compacted earth as a building material, Constr. Build. Mater. 110 (2016) 70–78.
[9] R.J. Chandler, C.I. Gutierrez, The filter paper method of suction measurement, Géotechnique 36 (1986) (1986) 265–268.
[10] R. Charlier, Approche unifiée de quelques problèmes non linéaires de mécanique des milieux continus par la méthode des éléments finis, Thèse de doctorat, Faculté des Sciences Appliquées, Université de Liège, 1987.
[11] F. Collin, X. Li, J.P. Radu, R. Charlier, Thermo-hydro-mechanical coupling in clay barriers, Eng. Geol. 64 (2002) 179–193.
[12] P. Delage, M. Howat, Y. Cui, The relationship between suction and swelling properties in a heavily compacted unsaturated clay, Eng. Geol. 50 (1–2) (1998) 31–48.
[13] M.C.J. Delgado, I.C. Guerrero, The selection of soils for unstabilised earth building: a normative review, Constr. Build. Mater. 21 (2) (2007) 237–251.
[14] D.C. Drucker, W. Prager, Solid mechanics and plastic analysis for limit design, Q. Appl. Math. 10 (2) (1952) 157–165.
[15] B. François, L. Laloui, ACMEG-TS: A constitutive model for unsaturated soils under non-isothermal conditions, Int. J. Numer. Anal. Methods Geomech. 32 (2008) 1955–1988.
[16] D.G. Fredlund, H. Rahardjo, Soil Mechanics for Unsaturated Soils, Wiley, New-York, 1993.
[17] D. Gallipoli, A.W. Bruno, C. Perlot, J. Mendes, A geotechnical perspective of raw earth building, Acta Geotech. (2017), http://dx.doi.org/10.1007/s11440-016-0521-1.
[18] P. Gerard, M. Mahdad, A.R. McCormack, B. François, A unified failure criterion for unstabilized rammed earth materials upon varying relative humidity conditions, Constr. Build. Mater. 95 (2015) 437–447.
[19] P. Gerard, R. Charlier, R. Chambon, F. Collin, Influence of evaporation and seepage on the convergence of a ventilated cavity, Water Resour. Res. 44 (5) (2008), http://dx.doi.org/10.1029/2007WR006500.
[20] M.R. Hall, Y. Djerbib, Rammed earth sample production: context, recommendations and consistency, Constr. Build. Mater. 18 (2004) 281–286.
[21] M. Hall, D. Allinson, Analysis of the hygrothermal functional properties of stabilised rammed earth materials, Build. Environ. 44 (9) (2009) 1935–1942.
[22] H. Houben, H. Guillaud, Earth construction – a comprehensive guide, Second ed., Intermediate Technology Publications, London, UK, 1994.
[23] J.C. Hujeux, Une loi de comportement pour le chargement cyclique des sols, in: Génie Parasismique, Les éditions de l'E.N.P.C, Paris, 1985, pp. 287–303.
[24] P.A. Jaquin, C.E. Augarde, D. Gallipoli, D.G. Toll, The strength of unstabilised rammed earth materials, Géotechnique 59 (5) (2009) 487–490.
[25] L. Laloui, M. Nuth, B. François, Mechanics of unsaturated soils, in: L. Laloui (Ed.), Mechanics of unsaturated materials, Wiley & Sons, Inc., 2010, pp. 29–54.
[26] B. Little, T. Morton, Building with earth in Scotland: innovative design and sustainability. Scottish Executive Central Research Unit Publication, 2001.
[27] L. Miccoli, D.V. Oliveira, R.A. Silva, U. Müller, L. Schueremans, Static behaviour of rammed earth: experimental testing and finite element modelling, Mater. Struct. 48 (10) (2015) 3443–3456.
[28] L. Miccoli, A. Drougkas, U. Müller, In-plane behaviour of rammed earth under cyclic loading: experimental testing and finite element modelling, Eng. Struct. 125 (2016) 144–152.
[29] G.F. Middleton, Bulletin 5. Earth Wall Construction. Fourth Edition, CSIRO Division of Building, Construction and Engineering, North Ryde, Australia, 1992.
[30] J.C. Morel, A. Mesbah, M. Oggero, P. Walker, Building houses with local materials: means to drastically reduce the environmental impact of construction, Build. Environ. 36 (2001) 1119–1126.
[31] H. Nowamooz, C. Chazallon, Finite element modelling of a rammed earth wall, Constr. Build. Mater. 25 (4) (2011) 2112–2121.
[32] M. Nuth, L. Laloui, Effective stress concept in unsaturated soils: clarification and validation of a unified framework, Int. J. Numer. Anal. Methods Geomech. 32 (7) (2008) 771–801.
[33] NZS 4298:1998, New Zealand Standard, Materials and Workmanship for Earth Buildings, Standard New Zealand, Wellington, New Zealand, 1998.
[34] L. Soudani, A. Fabbri, J.C. Morel, M. Woloszyn, P.A. Chabriac, H. Wong, A.C. Grillet, Assessment of the validity of some common assumptions in hygrothermal modeling of earth based materials, Energy Build. 116 (2016) 498–511.
[35] Standards Australia, The Australian Earth Building Handbook, Standards Australia, Sydney, Australia, 2002.
[36] M.T. Van Genuchten, A closed-form equation for predicting the hydraulic conductivity of unsaturated soils, Soil Sci. Soc. Am. J. 44 (1980) 892–898.
[37] P. Walker, R. Keable, J. Martin, V. Maniatidis, Rammed Earth: Design and Construction Guidelines, BRE Bookshop, Watford, UK, 2005.